Amyloid deposition in the hippocampus and entorhinal cortex: Quantitative analysis of a transgenic mouse model

John F. Reilly*, Dora Games†, Russell E. Rydel†, Stephen Freedman†, Dale Schenk†, Warren G. Young*, John H. Morrison*‡, and Floyd E. Bloom*§¶

*Neurome, Inc., La Jolla, CA 92037; †Elan Pharmaceuticals, South San Francisco, CA 94080; ‡Kastor Neurobiology of Aging Laboratories and Fishberg Research Center for Neurobiology, Mount Sinai School of Medicine, New York, NY 10029; and §Department of Neuropharmacology, The Scripps Research Institute, La Jolla, CA 92037

Contributed by Floyd E. Bloom, February 7, 2003

Various transgenic mouse models of Alzheimer's disease (AD) have been developed that overexpress mutant forms of amyloid precursor protein in an effort to elucidate more fully the potential role of β-amyloid (Aβ) in the etiopathogenesis of the disease. The present study represents the first complete 3D reconstruction of Aβ in the hippocampus and entorhinal cortex of PDAPP transgenic mice. Aβ deposits were detected by immunostaining and thioflavin fluorescence, and quantified by using high-throughput digital image acquisition and analysis. Quantitative analysis of amyloid load in hippocampal subfields showed a dramatic increase between 12 and 15 months of age, with little or no earlier detectable deposition. Three-dimensional reconstruction in the oldest brains visualized previously unrecognized sheets of Aβ coursing through the hippocampus and cerebral cortex. In contrast with previous hypotheses, compact plaques form before significant deposition of diffuse Aβ, suggesting that different mechanisms are involved in the deposition of diffuse amyloid and the aggregation into plaques. The dentate gyrus was the hippocampal subfield with the greatest amyloid burden. Sublaminar distribution of Aβ in the dentate gyrus correlated most closely with the termination of afferent projections from the lateral entorhinal cortex, mirroring the selective vulnerability of this circuit in human AD. This detailed temporal and spatial analysis of Aβ and compact amyloid deposition suggests that specific corticocortical circuits express selective, but late, vulnerability to the pathognomonic markers of amyloid deposition, and can provide a basis for detecting prior vulnerability factors.

Alzheimer's disease (AD), the most common form of dementia in the aging population, is characterized by the extracellular accumulation of β-amyloid (Aβ), the intracellular appearance of neurofibrillary tangles, and synaptic and neuronal loss (1). Mounting evidence supports a causal role for Aβ in the pathophysiology of AD (2, 3). Various transgenic models have been developed which overexpress mutant forms of amyloid precursor protein (APP); these models mimic some aspects of AD pathology, including Aβ deposition and synaptic damage (4–9).

In AD, amyloid deposition and neurofibrillary tangle formation occur in a spatially and temporally defined pattern in specific neocortical and hippocampal regions that reflects selective vulnerability of certain circuits, particularly corticocortical circuits in neocortex (10, 11) and the perforant path that projects from the entorhinal cortex (EC) to the dentate gyrus (DG) (12, 13). Transgenic mouse models that overexpress mutant APP show an age-dependent accumulation of Aβ (14); however, there has been no comprehensive quantitative analysis of the spatial and temporal progression of amyloid and Aβ accumulation, especially in the most vulnerable regions.

Deposits of Aβ that form in AD have been morphologically classified into several types, such as diffuse, fibrillar, dense-cored or classic, compact, or "burnt-out" (15, 16). Plaque formation is thought to progress from diffuse through compact (17–19), and the relative frequency of these types of deposits changes during the progression of AD, with diffuse plaques being prevalent in the preclinical stages, and fibrillar plaques increasing in frequency as the disease progresses to clinical dementia (15, 20). Different types of Aβ deposits also occur in transgenic mouse models of AD; morphological classifications include diffuse and compact. Compact deposits are frequently associated with neuritic changes (21). The relative distribution and temporal progression of diffuse versus compact amyloid has not been investigated in transgenic models.

In human AD, memory deficits associated with disease progression are likely to result from pathological changes in the EC and hippocampus, regions critical for formation of new memories and among the most severely affected in AD. In fact, the perforant path is the most vulnerable circuit in the cortex with respect to both aging and AD (22). There is recent experimental evidence from mouse models that this same neural circuit is implicated in amyloid deposition in transgenic models (23–25). The present study was undertaken to analyze quantitatively the distribution of diffuse and compact Aβ deposits over time in the PDAPP mouse model of AD, and determine the degree to which such patterns can be linked to the phenotype of selective vulnerability of the perforant path reflected in human AD.

Materials and Methods

Animals and Tissue Preparation. Heterozygous PDAPP transgenic mice carrying the APPV717F familial AD mutation (26) were bred from the previously established line PDAPP-109 over several generations on hybrid backgrounds representing combinations of C57BL/6, DBA, and Swiss–Webster strains (6, 14). Three mice were used at 6, 12, 15, 18, and 22 months of age, with an additional three mice at the oldest age for serial reconstruction. Animals were anesthetized with avertin (0.5 mg/g body weight) and transcardially perfused with normal saline followed by 4% paraformaldehyde. Brains were cryoprotected with 30% sucrose, frozen, and sectioned coronally at 50 μm on a sliding microtome.

Thioflavin Staining and Immunohistochemistry. For visualization of compact amyloid plaques, a systematic random series of brain sections was collected with 1 in 3 spacing (i.e., every third section from a complete series, with the starting section chosen at random), mounted on gelatin-subbed slides, stained with 0.01% thioflavin S (ICN), counterstained with propidium iodide, and coverslipped with SlowFade (Molecular Probes).

Total Aβ was detected by immunostaining a systematic ran-

Abbreviations: Aβ, β-amyloid; AD, Alzheimer's disease; APP, amyloid precursor protein; EC, entorhinal cortex; DG, dentate gyrus; ZnT3, zinc transporter 3; IML, inner molecular layer; MML, middle molecular layer; OML, outer molecular layer.

¶To whom correspondence should be addressed. E-mail: fbloom@neurome.com.

NEUROSCIENCE

dom series with 1 in 3 spacing using biotinylated monoclonal antibody 3D6 (14). This antibody is specific to amino acids 1–5 of Aβ, and does not recognize secreted or full-length APP. Free-floating sections were incubated with 3D6 (1.5 μg/ml) for 48 h, then with Alexa Fluor 546 streptavidin (2.5 μg/ml, Molecular Probes) for 24 h. Sections were mounted on gelatin-subbed slides and coverslipped with SlowFade with 4′,6-diamidino-2-phenylindole (Molecular Probes). All sections from an additional three 22-month-old animals were processed for serial reconstruction of Aβ deposits.

Sublayer borders within the DG were assessed in a systematic random series with 1 in 6 spacing. Free-floating sections were incubated with anti-zinc transporter 3 (ZnT3, 0.07 μg/ml; ref. 27) for 48 h, then with biotinylated goat anti-rabbit IgG (0.25 μg/ml, Jackson Immunoresearch) for 2 h. The signal was amplified by using streptavidin-HRP and the Alexa-488-tyramide signal amplification kit (Molecular Probes) or biotin-XX-tyramide signal amplification kit (Molecular Probes) followed by the ABC kit (Vector Laboratories). Sections were mounted on gelatin-subbed slides and coverslipped with SlowFade, or developed with diaminobenzidine (Vector Laboratories) then counterstained with propidium iodide, dehydrated, and coverslipped with DPX mountant (EM Science).

Image Acquisition and Data Analysis. Data collection was performed by using NEUROMOSAIC (Neurome, La Jolla, CA) software for high-throughput digital image acquisition, using a fully motorized Zeiss Axioplan 2ie microscope equipped with an AxioCam HRc and an eight-slide scanning stage. Signals from different fluorescent channels were acquired sequentially to allow subsequent registration of images. Entire sections composed of multiple image tiles were acquired at a final magnification of ×264, with the entire data set comprising ≈900 GB. Three-dimensional reconstruction of Aβ was performed by using AMIRA (TGS, Richmond, TX).

Quantitative analysis was performed by using NEUROLUCIDA (MicroBrightField, Williston, VT) and NIH IMAGE (Scion, Frederick, MD). Each structure was sampled throughout its entire anterior–posterior extent in a series of sections at 150-μm intervals. Random selection of the starting section relative to each structure ensured unbiased sampling according to the principles of modern stereology (28). The 1 in 3 interval used for analysis was previously determined to provide coefficients of error of <0.10 for each hippocampal and cortical subregion measured (data not shown). Structures were contoured on images of counterstained sections by using NEUROLUCIDA, and the Cavalieri principle (28) was used to estimate volumes of brain structures from the contoured areas. Images of thioflavin S and 3D6 staining from within the individual contours were digitally extracted and exported to NIH IMAGE (for example, see Fig. 3). The stained area was then determined by application of a gray-level threshold based on the intensity of background staining in control sections. Different thresholds were used for thioflavin S and 3D6, but for each stain the selected threshold was held constant across all animals and ages. Standardization of staining and imaging parameters permitted the uniform application of the threshold, though occasional manual editing of segmented images was required to remove staining artifacts. The Cavalieri principle was used to estimate amyloid volumes from stained areas, and amyloid load was calculated as volume of amyloid within each structure divided by the volume of the structure. Diffuse amyloid load was determined by subtracting the load of compact amyloid, detected with thioflavin S, from total amyloid load, detected with 3D6 immunostaining.

Statistical Analyses. All data were analyzed by using ANOVA. Statistical significance between regions and ages was determined by using a Bonferroni post hoc test.

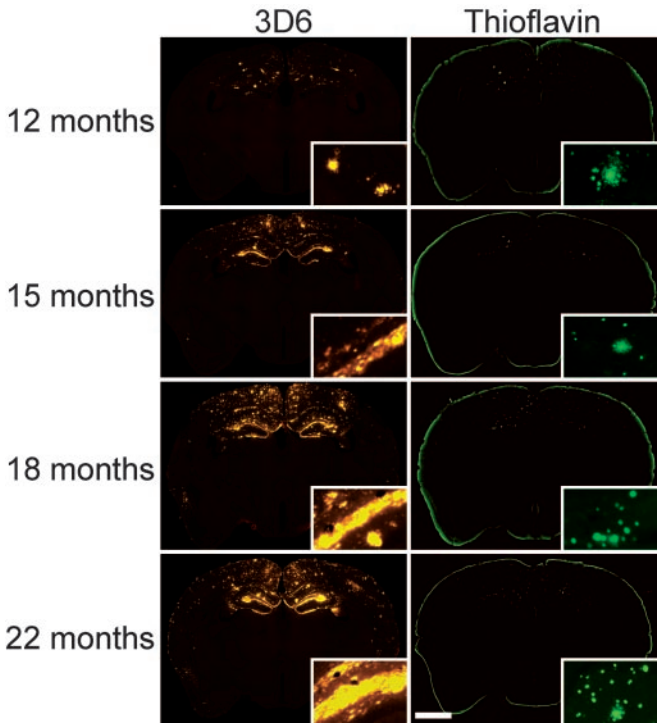

Fig. 1. Representative coronal sections of PDAPP transgenic mice. 3D6 immunostaining (*Left*) shows increasing Aβ deposition over time. Thioflavin staining (*Right*) demonstrates compact plaques at all ages examined. (*Insets*) Higher magnification of Aβ deposits. [Bar = 1.5 mm (150 μm for *Insets*).]

Results

Qualitative Analysis of Amyloid Accumulation. Minimal deposition of Aβ was evident at 6 months of age in PDAPP mice, the earliest time point in the present study. These early deposits were widely dispersed in the hippocampus and cingulate and retrosplenial cortices. The majority of Aβ deposits at this time point were thioflavin-positive with compact morphology. Amyloid deposition increased slightly by 12 months of age, after which a dramatic increase in the deposition of diffuse Aβ was observed (Fig. 1). Compact Aβ deposits were most prevalent in the hippocampus, cingulate and retrosplenial cortices, and the septum, and were also observed in primary motor cortex, primary and secondary visual cortices, and parietal association areas. The 3D6 antibody detects both diffuse and compact amyloid deposits. Double-labeling with thioflavin S and 3D6 demonstrated that thioflavin-positive deposits were entirely contained within areas of 3D6 immunoreactivity (data not shown). 3D6 immunoreactivity was prevalent in the hippocampus and most areas of cerebral cortex, as well as the lateral septal nucleus and the pontine gray matter. Staining was also observed in the granule cell layer of the olfactory bulb, the laterodorsal and rhomboid nuclei of the thalamus, and in selected white matter tracts, including the corpus callosum, fornix, and mammillothalamic tract. No amyloid deposits were detected in the cerebellum or brainstem, with the exception of the pontine gray matter.

To better appreciate the spatial distribution of Aβ in the brain, serial sections from 22-month-old animals immunostained with 3D6 were digitally reconstructed (Fig. 2). Substantially more Aβ deposition was evident in the hippocampus than in other brain regions. The 3D reconstruction revealed that Aβ deposits were not isolated elements but rather existed as sheets of Aβ coursing through the hippocampus and retrosplenial cortex. A continuum of Aβ was visible from the molecular layer of the DG through the stratum lacunosum-moleculare of the hippocampal CA1

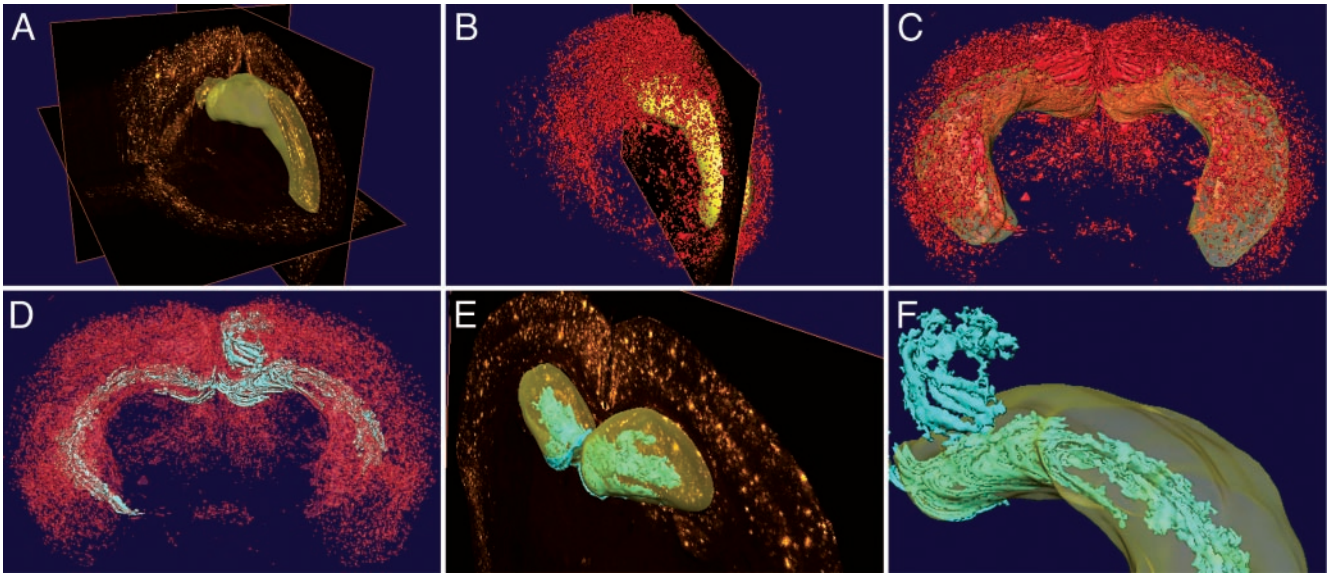

Fig. 2. Three-dimensional reconstruction of Aβ distribution. (*A*) Serial coronal sections immunostained with 3D6 were imaged and compiled into a 3D data file. A surface reconstruction of the hippocampus is shown in yellow. (*B*) Aβ deposits were segmented by thresholding and are displayed as a 3D reconstruction (red). A surface reconstruction of the hippocampus (yellow) and a single coronal section are shown for orientation. (*C*) Three-dimensional reconstruction of Aβ (red) viewed from the posterior aspect of the brain with the hippocampus shown as transparent yellow. Note the extensive deposition in the neocortex and hippocampus, and the central lucency representing the midbrain and caudate-putamen with punctate Aβ visible in the frontal cortex and olfactory bulb. (*D*) Large lakes and ribbons of Aβ (cyan) were identified by automated detection of contiguous structures within the 3D reconstruction of Aβ (shown as transparent red; same angle of view as *C*). (*E*) Aβ sheets (cyan) are visible in the rostral part of the DG, shown against a single coronal section, with the surface reconstruction of the hippocampus in transparent yellow. (*F*) Magnified view of the Aβ lakes and ribbons (cyan) in the DG (within the transparent yellow hippocampal surface) and extending into the retrosplenial cortex (above).

subfield and the fasciola cinerea. Animations of 3D reconstructions are available as Supporting Movies 1–3, which are published as supporting information on the PNAS web site, www.pnas.org.

Quantitative Analysis of Hippocampal Amyloid Loads. To elucidate more fully the progression of amyloid deposition in the hippocampus, diffuse and compact deposits were quantified at five ages ranging from 6 to 22 months in the four main hippocampal subfields: CA1 (including CA2), CA3, DG, and subiculum (Fig. 3). An ANOVA revealed a main effect of age on both diffuse ($F_{(4,15)} = 17.6$, $P < 0.0001$) and compact ($F_{(4,15)} = 17.9$, $P < 0.0001$) amyloid deposition. Post hoc tests demonstrated significant increases in diffuse Aβ at 15, 18, and 22 months compared with earlier time points, and significant increases in compact amyloid at all later ages compared with 6 months (complete results of pairwise comparisons are available in Tables 2–4, which are published as supporting information on the PNAS web site). At 6 months of age, amyloid load in all hippocampal subfields was <0.1%. At 12 months, loads ranged from 0.8 to 2.4%, with higher loads in CA1 and subiculum. At this time point, the majority of the Aβ deposits were of the compact type. Between 12 and 15 months, diffuse Aβ deposition increased dramatically in all subfields, particularly the DG, where the load reached 19%, with <1% compact amyloid. The subiculum load was 5.4%, with nearly half of the Aβ deposits being of the compact type. No further increases in DG or subiculum amyloid loads could be seen in the 18- and 22-month samples, but loads in CA1 and CA3 continued to increase progressively, reaching 13.4% and 16.9%, respectively. Aβ load in the DG was significantly greater than all other subregions at 15, 18, and 22 months. The volume of the hippocampus did not change with age or amyloid deposition, nor did the volumes of individual subfields (Table 1).

Based on the quantitatively highest amyloid load in the DG, and the observation that Aβ appeared to be distributed in a specific laminar pattern, a more detailed quantitative analysis of the Aβ load in the DG of 22-month-old animals was performed. To facilitate accurate determination of the laminar borders within the molecular layer of the DG, immunostaining for ZnT3 was used. Within the DG, ZnT3 immunoreactivity is present in the hilus, the inner molecular layer (IML), and the outer molecular layer (OML), and absent from the granule cell layer and the middle molecular layer (MML). Aβ immunoreactivity showed substantial colocalization with ZnT3 (Fig. 4). Quantitative analysis of total Aβ load in the sublayers of the DG demonstrated that loads were highest in the IML and OML, with ≈45% of the volume of those sublayers containing Aβ deposits. The MML showed <7% amyloid load. The vast majority of the amyloid in all sublayers was diffuse, with <2.3% compact amyloid present in any layer (data not shown).

Circuit-Specific Accumulation of Aβ. The pattern of amyloid within the molecular layer of the DG suggests a correlation between Aβ deposition and the underlying neural circuitry. The dentate molecular layer receives both extrinsic and intrinsic projections; inputs to the OML and MML derive from the lateral and medial entorhinal cortices, respectively, and input to the IML derives from the dentate hilus (Fig. 5), with limited projections from the contralateral DG (29). To examine Aβ deposition in regions that project into the DG, total Aβ load was quantified in the lateral and medial entorhinal cortices in 6- to 22-month-old animals. Nearly all of the Aβ deposits were diffuse, with compact amyloid loads <0.2% in both regions at all ages examined (data not shown). Aβ was observed in all layers of the lateral EC, with a discontinuous but distinct band of deposition seen in layer II, especially at 15 months of age. An ANOVA revealed a main effect of age ($F_{(4,15)} = 6.9, P < 0.001$) on amyloid load (complete results of pairwise comparisons are available in Table 5, which is published as supporting information on the PNAS web site).

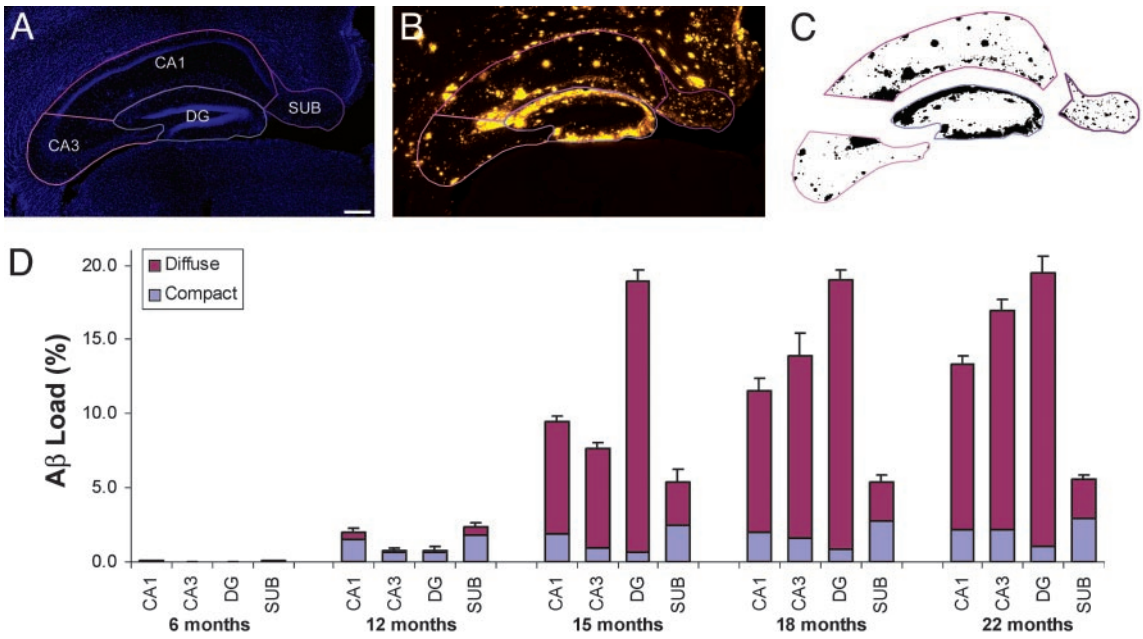

Fig. 3. Quantitative analysis of hippocampal Aβ load. (*A*) Hippocampal subfields, including CA1, CA3, DG, and subiculum (SUB) were contoured on 4′,6-diamidino-2-phenylindole-counterstained sections. (Bar = 200 μm.) (*B*) Contours were applied to the images of 3D6-immunostaining on the same sections. Contours on propidium iodide-counterstained sections were applied to thioflavin S-stained sections (data not shown). (*C*) A uniform threshold based on staining of control sections was applied to each subfield, and the area occupied by amyloid was determined. (*D*) Aβ load in hippocampal subfields over time. Total and compact load were calculated as the volume fractions of 3D6 and thioflavin staining, respectively, and diffuse load was determined by subtraction of compact from total. Data were analyzed by ANOVA; Tables 2–4 present complete results of pairwise comparisons.

Total Aβ loads before 15 months of age were negligible. From 15 to 22 months, there was a progressive increase in diffuse Aβ deposition in the lateral EC to a maximum of 16.4%, whereas loads in the medial EC remained below 2.3%. This demonstrates a circuit-specific accumulation of Aβ that preferentially involves the lateral perforant path, reflected by high levels in the lateral EC and its terminal zone, the OML, and low levels in the medial EC and its terminal zone, the MML. The discontinuous band of Aβ deposits seen in layer II of the lateral EC is coincident with the neurons that give rise to the lateral perforant path.

Discussion

The present study represents a comprehensive 3D analysis of amyloid burden in the hippocampus and EC in a mouse model of AD. Several transgenic mouse models that overexpress mutant APP have been generated, including PDAPP (6), Tg2576 (30), and APP23 (9). In general, the qualitative temporal and spatial distribution of Aβ is similar among these three lines, but no other quantitative histological data have yet been reported. Immunoreactive deposits are first detected at 5–6 months of age, and by 18–24 months of age the amyloid burden is pronounced. Notable differences between the lines include substantial cerebrovascular amyloid in the APP23 line (31), and the formation of "giant plaques" in Tg2576 mice (32). The localization, extent, and morphology of Aβ deposits in transgenic models vary depending on the promoter construct and the genetic background of the mice (4–9). Despite detailed biochemical quantitation of Aβ levels over time in these transgenic lines (14, 33, 34), nearly all of the histological analyses have been qualitative. This study quantitatively confirms earlier data suggesting that the DG and EC are primary sites of amyloid deposition in PDAPP mice (14, 25, 35). This same circuit is among the earliest to show demonstrable pathology in human AD (12, 13, 22, 36), and pathological changes in this circuit are likely to be causally related to the clinical symptoms of AD. Thus, the data presented here support the validity of the PDAPP mouse model of AD with respect to the selective vulnerability of the perforant path. The importance of the perforant path for Aβ accumulation was

Table 1. Volumes of hippocampal subfields and associated amyloid volumes

	6 mo.	12 mo.	15 mo.	18 mo.	22 mo.
Volume, mm^3					
CA1/CA2	6.7 ± 0.6	7.0 ± 0.1	6.1 ± 1.3	6.2 ± 0.5	6.7 ± 0.6
CA3	4.2 ± 0.6	3.8 ± 0.2	4.2 ± 0.6	4.1 ± 0.2	4.4 ± 0.4
DG	4.1 ± 0.3	4.9 ± 0.3	4.7 ± 0.4	4.7 ± 0.1	4.5 ± 0.2
Subiculum	3.0 ± 0.2	2.9 ± 0.1	3.1 ± 0.4	3.0 ± 0.1	3.4 ± 0.2
HC	18.1 ± 1.6	18.6 ± 0.7	18.1 ± 2.3	18.0 ± 1.0	18.8 ± 1.7
Total amyloid volume, μm^3					
CA1/CA2	3 ± 1	142 ± 22	481 ± 91	703 ± 99	922 ± 35
CA3	0 ± 0	31 ± 7	241 ± 50	472 ± 8	620 ± 50
DG	1 ± 1	38 ± 5	860 ± 34	899 ± 33	816 ± 73
Subiculum	1 ± 1	69 ± 6	141 ± 34	145 ± 6	171 ± 12

Results are presented as mean ± SEM. HC, hippocampus; sum of the four listed subfields.

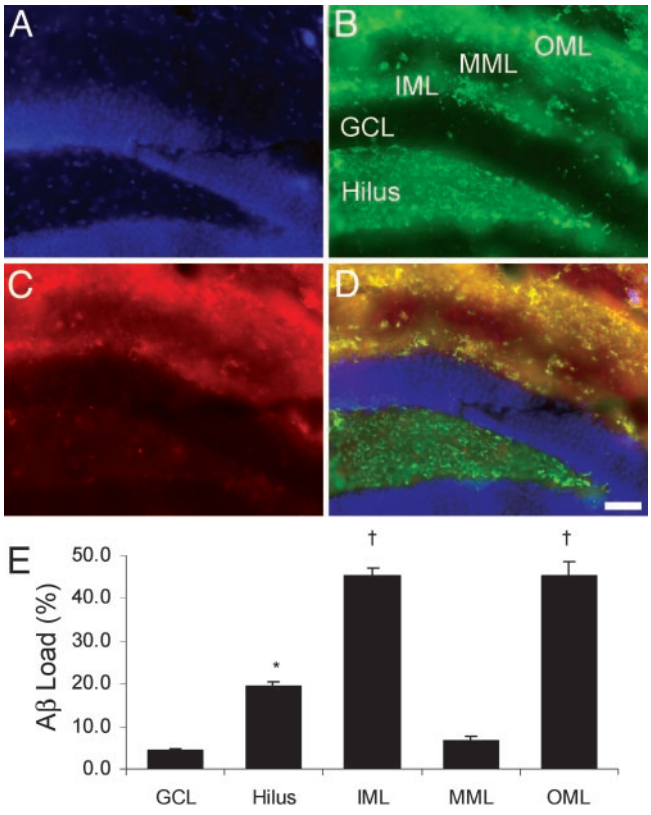

Fig. 4. Aβ load in DG sublayers. (*A–D*) Triple-fluorescent image of the DG, showing nuclear counterstaining (4′,6-diamidino-2-phenylindole, *A*), ZnT3 (*B*) with the hilus, granule cell layer (GCL), IML, MML, and OML indicated, and 3D6 (*C*). Yellow bands in IML and OML in the merged image (*D*) indicate extensive overlap of amyloid deposition with ZnT3 labeling of perforant path (OML) and hilus (IML) terminations. (Bar = 50 μm.) (*E*) Total Aβ load in DG sublaminae in 22-month-old animals. Compact load was <1.5% in all sublayers (data not shown). *, $P < 0.005$ vs. GCL and MML; †, $P < 0.0001$ vs. hilus, GCL, and MML.

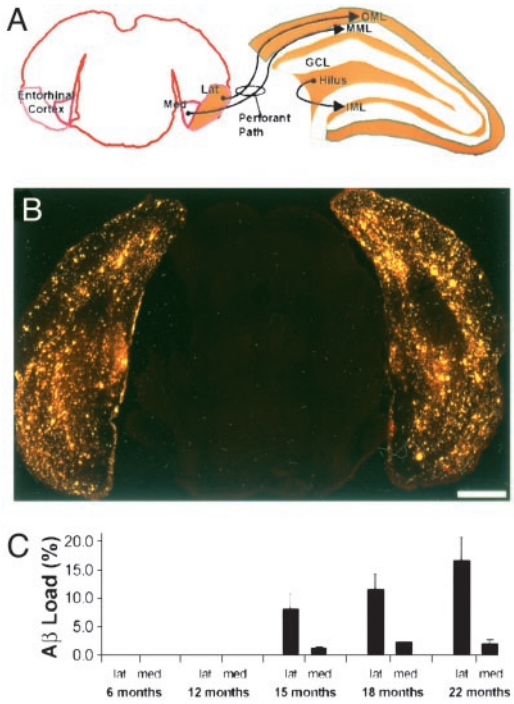

Fig. 5. Aβ load in the EC. (*A*) Diagram of the major extrinsic and intrinsic afferents of the DG, showing the projection of lateral EC to OML and medial EC to MML. (*B*) Representative coronal sections showing 3D6 immunostaining at 22 months of age. (Bar = 1.0 mm.) (*C*) Total Aβ load in the EC over time. Compact load was <0.2% in both subregions (data not shown). Data were analyzed by ANOVA; Table 5 presents complete results of pairwise comparisons.

recently demonstrated experimentally in transgenic mouse models of AD, where Aβ deposition in the DG was decreased by perforant path lesions, suggesting that deposition results from axonal transport of APP from the EC to terminal fields in the DG (23, 24).

The rapid accumulation of Aβ in both the OML of the DG and the lateral EC, beginning after 12 months of age in PDAPP mice, indicates that the origin and terminations of the lateral perforant path are far more selectively vulnerable to amyloid deposition that the medial perforant path, and suggests that the lateral perforant path is predisposed to Aβ accumulation from a younger age. This hypothesis is supported by recent data demonstrating a hippocampal volume reduction in PDAPP mice compared with wild-type littermates at 3 months of age, well before significant deposition of amyloid in the brain (37). Additional evidence in support of pathological changes occurring before Aβ deposition includes neurochemical, electrophysiological, behavioral, and metabolic changes in young transgenic animals (7, 38–42).

In previous data from magnetic resonance microscopy, no change in hippocampal volume in transgenic mice was observed from 3 to 22 months of age (37), consistent with the data from the present study. It is interesting that despite the dramatic increase in amyloid burden from 12 to 22 months of age in these animals, no apparent increase in volume is detected. This finding is consistent with the hypothesis that diffuse amyloid is not space-filling. It has been shown that compact deposits do displace neuronal elements (43), and apical dendrites in CA1 can be seen passing around thioflavin-positive plaques by using confocal microscopy (J.F.R., unpublished observations). The volume occupied by compact amyloid is insufficient to produce a detectable volume change in the hippocampus or individual subfields even at the oldest age examined.

The quantitative analyses performed in the present study used image analysis in conjunction with the sampling principles of stereology. These techniques represent a significant departure from the way amyloid deposition has traditionally been measured, considering only selected fields in a small number of brain sections deemed as representative. A direct comparison of selective sampling with stereological methods that employ systematic random sampling has demonstrated that the former may lead to unreliable estimates of amyloid burden (44).

Analysis of compact and diffuse Aβ deposits in PDAPP mice revealed that significant amounts of compact plaques are present in the hippocampus at 12 months of age, before the accumulation of diffuse Aβ. Traditionally, the formation of individual plaques has been thought to follow a progression from diffuse to classic to compact (17–19). More recent evidence, both experimental and theoretical, has begun to suggest that different types of Aβ deposits may form independently (20, 45, 46). The data from the present study support the hypothesis of independent formation of different morphological types of deposits, rather than the evolution of diffuse into compact deposits.

The relative proportion of the different classes of Aβ deposits is potentially of great clinical importance, because they may be associated with different levels of toxicity. Neuronal damage has been correlated with fibrillar plaques (15, 47), and this is supported by *in vitro* data (48). However, recent evidence suggests that soluble forms of Aβ are also highly toxic, and may be more directly responsible for the pathophys-

iological changes in AD (49–51). Longitudinal *in vivo* imaging studies in Tg2576 mice have shown that compact plaques develop to a given size then remain stable for months, with ongoing formation of new compact plaques and only occasional regression of existing deposits (52), consistent with what has been hypothesized for amyloid deposits in human AD (53). These data are consistent with the progression of compact amyloid accumulation in PDAPP mice observed in the present study. No data on the stability of diffuse Aβ deposits are available, but if these deposits are in equilibrium with soluble, oligomeric forms of Aβ, diffuse Aβ represents a large pool of potentially neurotoxic molecules.

The present study quantifies amyloid accumulation in a mouse model of AD and suggests a pattern of selective vulnerability highly reminiscent of that present in AD, validating the use of these models for evaluation of novel therapeutic strategies aimed at decreasing the Aβ burden in the brain. The high-throughput digital quantitative analyses used in these studies provide rapid methods for identification of likely targets for therapeutic intervention and reliable assessment of the efficacy of potential treatments.

We thank Dr. Richard D. Palmiter for the anti-ZnT3 antibody; Brian Baumann for software engineering work on NeuroMosaic; Dr. Jeff M. Redwine for assistance with the 3D reconstruction; Anna Cervantes, Denise Cuizon, Tiffany Loui, and Faisal Chawla for excellent technical assistance; and Drs. Patrick R. Hof and Ron S. Broide for helpful comments on the manuscript.

1. Price, D. L. & Sisodia, S. S. (1998) *Annu. Rev. Neurosci.* **21,** 479–505.
2. Hardy, J. & Selkoe, D. J. (2002) *Science* **297,** 353–356.
3. Sommer, B. (2002) *Curr. Opin. Pharmacol.* **2,** 87–92.
4. Masliah, E. & Rockenstein, E. (2000) *J. Neural. Transm.* (Suppl.) **59,** 175–183.
5. Dodart, J. C., Mathis, C., Saura, J., Bales, K. R., Paul, S. M. & Ungerer, A. (2000) *Neurobiol. Dis.* **7,** 71–85.
6. Games, D., Adams, D., Alessandrini, R., Barbour, R., Berthelette, P., Blackwell, C., Carr, T., Clemens, J., Donaldson, T., Gillespie, F., *et al*. (1995) *Nature* **373,** 523–527.
7. Hsia, A. Y., Masliah, E., McConlogue, L., Yu, G. Q., Tatsuno, G., Hu, K., Kholodenko, D., Malenka, R. C., Nicoll, R. A. & Mucke, L. (1999) *Proc. Natl. Acad. Sci. USA* **96,** 3228–3233.
8. Moechars, D., Dewachter, I., Lorent, K., Reversé, D., Baekelandt, V., Naidu, A., Tesseur, I., Spittaels, K., Haute, C. V., Checler, F., *et al.* (1999) *J. Biol. Chem.* **274,** 6483–6492.
9. Sturchler-Pierrat, C., Abramowski, D., Duke, M., Wiederhold, K. H., Mistl, C., Rothacher, S., Ledermann, B., Burki, K., Frey, P., Paganetti, P. A., *et al*. (1997) *Proc. Natl. Acad. Sci. USA* **94,** 13287–13292.
10. Rogers, J. & Morrison, J. H. (1985) *J. Neurosci.* **5,** 2801–2808.
11. Pearson, R. C., Esiri, M. M., Hiorns, R. W., Wilcock, G. K. & Powell, T. P. (1985) *Proc. Natl. Acad. Sci. USA* **82,** 4531–4534.
12. Hyman, B. T., Van Hoesen, G. W., Damasio, A. R. & Barnes, C. L. (1984) *Science* **225,** 1168–1170.
13. Gómez-Isla, T., Price, J. L., McKeel, D. W., Jr., Morris, J. C., Growdon, J. H. & Hyman, B. T. (1996) *J. Neurosci.* **16,** 4491–4500.
14. Johnson-Wood, K., Lee, M., Motter, R., Hu, K., Gordon, G., Barbour, R., Khan, K., Gordon, M., Tan, H., Games, D., *et al.* (1997) *Proc. Natl. Acad. Sci. USA* **94,** 1550–1555.
15. Dickson, T. C. & Vickers, J. C. (2001) *Neuroscience* **105,** 99–107.
16. Yamaguchi, H., Hirai, S., Morimatsu, M., Shoji, M. & Ihara, Y. (1988) *Acta Neuropathol.* **76,** 541–549.
17. Rozemüller, J. M., Eikelenboom, P., Stam, F. C., Beyreuther, K. & Masters, C. L. (1989) *J. Neuropathol. Exp. Neurol.* **48,** 674–691.
18. Tagliavini, F., Giaccone, G., Frangione, B. & Bugiani, O. (1988) *Neurosci. Lett.* **93,** 191–196.
19. Terry, R. D. & Davies, P. (1980) *Annu. Rev. Neurosci.* **3,** 77–95.
20. Thal, D. R., Rüb, U., Schultz, C., Sassin, I., Ghebremedhin, E., Del Tredici, K., Braak, E. & Braak, H. (2000) *J. Neuropathol. Exp. Neurol.* **59,** 733–748.
21. Masliah, E., Sisk, A., Mallory, M., Mucke, L., Schenk, D. & Games, D. (1996) *J. Neurosci.* **16,** 5795–5811.
22. Morrison, J. H. & Hof, P. R. (1997) *Science* **278,** 412–419.
23. Sheng, J. G., Price, D. L. & Koliatsos, V. E. (2002) *J. Neurosci.* **22,** 9794–9799.
24. Lazarov, O., Lee, M., Peterson, D. A. & Sisodia, S. S. (2002) *J. Neurosci.* **22,** 9785–9793.
25. Su, Y. & Ni, B. (1998) *J. Neurosci. Res.* **53,** 177–186.
26. Murrell, J., Farlow, M., Ghetti, B. & Benson, M. D. (1991) *Science* **254,** 97–99.
27. Palmiter, R. D., Cole, T. B., Quaife, C. J. & Findley, S. D. (1996) *Proc. Natl. Acad. Sci. USA* **93,** 14934–14939.
28. Mouton, P. R. (2002) *Principles and Practices of Unbiased Stereology* (Johns Hopkins Univ. Press, Baltimore).
29. Blasco-Ibañez, J. M. & Freund, T. F. (1997) *Hippocampus* **7,** 307–320.
30. Hsiao, K., Chapman, P., Nilsen, S., Eckman, C., Harigaya, Y., Younkin, S., Yang, F. & Cole, G. (1996) *Science* **274,** 99–102.
31. Calhoun, M. E., Burgermeister, P., Phinney, A. L., Stalder, M., Tolnay, M., Wiederhold, K. H., Abramowski, D., Sturchler-Pierrat, C., Sommer, B., Staufenbiel, M. & Jucker, M. (1999) *Proc. Natl. Acad. Sci. USA* **96,** 14088–14093.
32. Sasaki, A., Shoji, M., Harigaya, Y., Kawarabayashi, T., Ikeda, M., Naito, M., Matsubara, E., Abe, K. & Nakazato, Y. (2002) *Virchows Arch.* **441,** 358–367.
33. Kawarabayashi, T., Younkin, L. H., Saido, T. C., Shoji, M., Ashe, K. H. & Younkin, S. G. (2001) *J. Neurosci.* **21,** 372–381.
34. Kuo, Y. M., Beach, T. G., Sue, L. I., Scott, S., Layne, K. J., Kokjohn, T. A., Kalback, W. M., Luehrs, D. C., Vishnivetskaya, T. A., Abramowski, D., *et al.* (2001) *Mol. Med.* **7,** 609–618.
35. Irizarry, M. C., Soriano, F., McNamara, M., Page, K. J., Schenk, D., Games, D. & Hyman, B. T. (1997) *J. Neurosci.* **17,** 7053–7059.
36. Braak, H. & Braak, E. (1999) in *Neurodegenerative and Age-Related Changes in Cerebral Cortex*, eds. Peters, A. & Morrison, J. H. (Kluwer Academic/Plenum, New York), Vol. 14, pp. 475–512.
37. Redwine, J. M., Kosofsky, B., Jacobs, R. E., Games, D., Reilly, J. F., Morrison, J. H., Young, W. G. & Bloom, F. E. (2003) *Proc. Natl. Acad. Sci. USA* **100,** 1381–1386.
38. Bednar, I., Paterson, D., Marutle, A., Pham, T. M., Svedberg, M., Hellström-Lindahl, E., Mousavi, M., Court, J., Morris, C., Mohammed, P. E., *et al*. (2002) *Mol. Cell. Neurosci.* **20,** 354–365.
39. Fodero, L. R., Sáez-Valero, J., McLean, C. A., Martins, R. N., Beyreuther, K., Masters, C. L., Robertson, T. A. & Small, D. H. (2002) *J. Neurochem.* **81,** 441–448.
40. Huitrón-Reséndiz, S., Sánchez-Alavez, M., Gallegos, R., Berg, G., Crawford, E., Giacchino, J. L., Games, D., Henriksen, S. J. & Criado, J. R. (2002) *Brain Res.* **928,** 126–137.
41. Larson, J., Lynch, G., Games, D. & Seubert, P. (1999) *Brain Res.* **840,** 23–35.
42. Sánchez-Alavez, M., Gallegos, R., Kalafut, M., Games, D., Henriksen, S. & Criado, J. (2002) *Neurosci. Lett.* **330,** 45–48.
43. Le, R., Cruz, L., Urbanc, B., Knowles, R. B., Hsiao-Ashe, K., Duff, K., Irizarry, M. C., Stanley, H. E. & Hyman, B. T. (2001) *J. Neuropathol. Exp. Neurol.* **60,** 753–758.
44. Bussière, T., Friend, P. D., Sadeghi, N., Wicinski, B., Lin, G. I., Bouras, C., Giannakopoulos, P., Robakis, N. K., Morrison, J. H., Perl, D. P. & Hof, P. R. (2002) *Neuroscience* **112,** 75–91.
45. Urbanc, B., Cruz, L., Buldyrev, S. V., Havlin, S., Irizarry, M. C., Stanley, H. E. & Hyman, B. T. (1999) *Biophys. J.* **76,** 1330–1334.
46. Armstrong, R. A. (1998) *Dement. Geriatr. Cogn. Disord*. **9,** 227–238.
47. Selkoe, D. J. (1994) *Annu. Rev. Neurosci.* **17,** 489–517.
48. Small, D. H., Mok, S. S. & Bornstein, J. C. (2001) *Nat. Rev. Neurosci.* **2,** 595–598.
49. Kim, H. J., Chae, S. C., Lee, D. K., Chromy, B., Lee, S. C., Park, Y. C., Klein, W. L., Krafft, G. A. & Hong, S. T. (2003) *FASEB J.* **17,** 118–120.
50. Klein, W. L., Krafft, G. A. & Finch, C. E. (2001) *Trends Neurosci.* **24,** 219–224.
51. Wang, H. W., Pasternak, J. F., Kuo, H., Ristic, H., Lambert, M. P., Chromy, B., Viola, K. L., Klein, W. L., Stine, W. B., Krafft, G. A. & Trommer, B. L. (2002) *Brain Res.* **924,** 133–140.
52. Christie, R. H., Bacskai, B. J., Zipfel, W. R., Williams, R. M., Kajdasz, S. T., Webb, W. W. & Hyman, B. T. (2001) *J. Neurosci.* **21,** 858–864.
53. Hyman, B. T., Marzloff, K. & Arriagada, P. V. (1993) *J. Neuropathol. Exp. Neurol.* **52,** 594–600.